Dalton Transactions

Synthesis, Structure, and Magnetism of BCC $KIrO_3$

Journal:	*Dalton Transactions*
Manuscript ID	DT-ART-05-2020-001836.R1
Article Type:	Paper
Date Submitted by the Author:	26-Jul-2020
Complete List of Authors:	Guo, Shu; Princeton University Powderly, Kelly; Princeton University Cava, Robert; Princeton University, Department of Chemistry

Synthesis, Structure, and Magnetism of BCC $KIrO_3$

Shu Guo, Kelly M. Powderly and R.J. Cava*

Department of Chemistry, Princeton University, Princeton, New Jersey 08544, USA

ABSTRACT

$KIrO_3$ in the body-centered cubic variant of the $KSbO_3$-type structure is reported. Black cube-shaped single crystals, obtained from the solid-state reaction in a half-closed silver capsule in a sealed quartz tube, were used for the structural characterization by single-crystal X-ray diffraction. The material, space group *Im*-3 (No. 204), exhibits a disordered K array and a three-dimensional (3D) IrO_6-based tunnel-like framework. Temperature-dependent magnetization and heat capacity measurements suggest a paramagnetic state for $KIrO_3$, with significant contribution of temperature independent paramagnetism and without any sign of long-range magnetic ordering (down to 1.8 K). The 3D motif of this material, based on the 5*d* Ir^{5+} ion, is of interest for investigating unconventional magnetism.

KEYWORDS (Spin-orbit coupling, Iridate, $KSbO_3$-type, 5*d* transition elements)

INTRODUCTION

In 3*d* transition metal oxide systems, localized orbitals and electron correlations frequently dominate the physical properties[1, 2]. Compared with 3*d* transition metals, the relatively large 5*d* orbitals can give rise to large electronic band width, large crystalline electric field splitting, and enhanced spin-orbit coupling (SOC). With SOC being strong in 5*d* systems, the physical properties are often totally different from those in 3*d* or 4*d* systems[3-5]. Hence, 5*d* transition metal oxides have received significant recent attention due to their physical properties, which can be challenging to explain.

From the viewpoint of structural dimensionality, 5*d* transition metal-based compounds can be classified into 0D (isolated polyhedra), 1D (chains or ribbons), 2D (layered sheet), or 3D (framework) structural types. In 0D systems, the magnetic atoms are relatively isolated and of less interest. In 1D systems, the polyhedra are usually connected with each other via corner-, edge-, or face-sharing, constructing chain-like or ribbon-like structures[6, 7]. Among 2D systems, the honeycomb lattice hosts some of the most popular SOC-dominated materials, such as α- and β-Li_2IrO_3[8, 9], Cu_2IrO_3[10, 11], Na_2IrO_3[12], and $Sr_3CaIr_2O_9$[13]. When considering 3D frameworks, more structural types are available, such as pyrochlore[14-16], spinel[17, 18], and the tunnel-like $KSbO_3$-type structural motif[19-24]. Among 3D systems, $KSbO_3$-type materials, which are typically ternary oxides, are a "hidden" resource for researchers. When 5*d* elements and this tunnel-like motif are combined, different kinds of strongly correlated systems are possible.

In particular, iridates have received a lot of attention recently due to the various electron configurations that are possible for iridium. Among them, Ir^{5+} ($5d^4$) is supposed to be a $J_{eff} = 0$ non-magnetic ground state with zero net moment. Interestingly, small magnetic moments have

been observed for many Ir^{5+} compounds[25]. In some perovskites, the local distortion of the IrO_6 octahedra contributes to the $J_{eff} \neq 0$ states[26]. Other researchers provide possible explanations for the observed magnetic moments in Ir^{5+}, such as large bandwidth, Ir-Ir hopping and noncubic crystal field that competes with the effective atomic SOC[27]. Therefore, Ir^{5+}-based materials are worthy of both experimental and theoretical study. Motivated by the ideas above, we have focused on 5*d*-element-based $KSbO_3$-type materials and have synthesized a new polymorph of the $KSbO_3$-type family, body-centered cubic (BCC) $KIrO_3$, via the solid-state reaction. Structurally, this material exhibits a 3D IrO_6-based tunnel-like network. The crystal structure is unambiguously body centered cubic, with disordered K in the tunnels, which contrasts with a simple cubic variant, with ordered K within the tunnels, that was previously reported[24]; a difference that may be attributed to different synthetic conditions. This body-centered vs. primitive structural character, based on the distribution of the alkali ions in the tunnels, is well known for $KSbO_3$-type materials[28]. Temperature-dependent magnetization reveals the presence of a small effective magnetic moment on the Ir ion, typical of that for Ir^{5+} compounds, and the magnetization and specific heat measurements reveal the absence of long-range magnetic ordering between 1.8 and 300 K. Our results expand the family of $KSbO_3$-type materials and suggest that a low temperature magnetic liquid state may be possible for $KIrO_3$.

EXPERIMENTAL

A non-stoichiometric ratio (molar ratio 2.5:1) of KO_2 to IrO_2 was used for the solid-state synthesis of the polycrystalline sample. The excess KO_2 was added to compensate for potential K loss during the reaction process. Considering the water-sensitivity of KO_2, all the raw materials were weighed and ground in a glovebox. The mixture was loaded into a silver tube with one end open and put in a quartz glass tube. The tube was sealed under vacuum and heated to 700 ℃ in a box furnace and

held for 4 days, after which it was quenched in ice water. The pure powder sample was obtained by washing the excess K_2O away with anhydrous ethanol. The final product was black powder. Small cubic single crystals could be found in the black solid (Figure 1*a*). The high-pressure synthesis experiment (6 GPa, 700 °C for 1.5 h) was performed in a cubic multi-anvil system (Rockland Research Corp.). A KO_2 plus IrO_2 mixture (molar ratio 1.5:1) was prepared under an Ar atmosphere and packed into a gold crucible, which was sealed, placed in a boron-nitride crucible, and prepared in the cubic assembly. After the synthesis step, the sample was quenched to room temperature and then depressurized.

A cubic single crystal (0.028 × 0.024 × 0.020 mm^3) was used for the single-crystal X-ray diffraction (S-XRD) experiment. The S-XRD data were obtained at 100(1) K via a Bruker D8 VENTURE diffractometer equipped with a PHOTON CMOS detector using graphite-monochromatized Mo-Kα radiation (λ = 0.71073 Å). The structure was solved by the direct methods by using the ShelXT structure solution program[29] and refined by using the XL refinement package within the Olex2 program[30, 31]. Additional symmetry was ruled out by the ADDSYM algorithm in the program PLATON[32]. The partial potassium difference Fourier maps were generated via the program PLATON. Powder diffraction (P-XRD) patterns were obtained with Cu Kα radiation at ambient temperature on a linear detector-equipped Bruker D8 Advance Eco diffractometer. The sample purity was checked via the consistency between the P-XRD pattern and simulated pattern from the S-XRD (Figure 1*b*).

DC magnetization data for $KIrO_3$ were collected via a VSM option-equipped Dynacool physical property measurement system (PPMS) from Quantum Design. A polycrystalline sample of BCC $KIrO_3$ was used for DC magnetic susceptibility collection within the temperature range T = 1.8-

300 K at an applied field H = 10,000 Oe (1T). M/H is used to define the susceptibility, where M is referring to the magnetization in emu, and H is referring to the applied field in Oe. Field-dependent magnetization characterization of BCC $KIrO_3$ was performed at 2 K and 300 K between 0 kOe and 90 kOe applied fields. A compressed pellet was used for heat capacity measurements (1.8-300 K) in the same PPMS instrument.

RESULTS AND DISCUSSION

The S-XRD structural analysis at 100 K revealed that our material crystallizes in the body centered cubic crystal system with space group *Im*-3 (No. 204). According to the S-XRD refinement results, one unique Ir atom (Wyckoff site 12*e*), two unique K atoms (Wyckoff sites 16*f* and 8*c*), and two unique O atoms (Wyckoff sites 12*d* and 24*g*) are found in the asymmetric unit. The crystal structure of BCC $KIrO_3$ is shown in Figure 2. It belongs to the $KSbO_3$-type structural family, which has intersecting [111] type tunnels. Each Ir atom is bonded to six O atoms to construct an IrO_6 octahedron. The IrO_6 octahedra are interconnected via edge-sharing O atoms to form Ir_2O_{10} dimers (Figure 2*a*). The Ir_2O_{10} dimers are connected to each other by corner-shared O atoms (Figure 2*b*) to construct a dimer-based framework that generates the alkali-containing tunnels (Figures 2*c* and 2*d*). The K atoms are distributed in the tunnels and exhibit a disordered state. The distance between nearest neighbor Ir atoms is 2.97 Å within the dimers, with no sign of direct metal-metal bonding. The Ir−O bond lengths are in the range of 1.94 to 1.97 Å. A Bond Valence Sum (BVS) calculation for Ir was performed and gives the result of +5.3, which is, within the uncertainties of BVS analysis in a multi-cation system, close to the ideal value of 5+. The determined composition, which includes large amounts of electropositive K+1 and electronegative O-2 fixes the formal oxidation sate of the transition metal Ir at 5+. Relevant single-crystal refinement results and crystallographic data are summarized in Tables 1-2.

To support the assignment of the body-centered cubic cell, the *hk0*, *hk1* and *hk2* reciprocal lattice planes, based on the S-XRD data, were inspected in detail. These reciprocal lattice planes are pictured in Figure 3. The body-centered cubic structure of $KIrO_3$ is illustrated by the systematic absence of *hkl* reflections when $h + k + l = 2n + 1$ (n = integer)[33]. The reflections circled in Figure 3 all meet the requirement of $h + k + l = 2n$. Critically, to distinguish *Pn*-3 from *Im*-3, no reflections in the *hk1* or *hk2* reciprocal lattice planes violate the $h + k + l = 2n$ requirement for body centering. Specifically, the insets show the absence of reflections at the 531 and 542 positions, which, in the report of primitive $KIrO_3$[24], were two of the strongest reflections said to support the evidence of a primitive cell (while the third reflection, the 221, is in an ambiguous position in our single-crystal images.) To evaluate the distribution of the K atoms in the tunnels, we created a difference Fourier map by deleting all the K atoms from the structural model using our diffraction data. The distribution of residual density in the [111] tunnels is shown in Figure 4, which clearly shows the presence of two independent positions for the K atoms in the tunnels. We assigned K atoms at these two positions with unconstrained occupancies and anisotropic thermal displacement parameters. The final potassium contents of the K1 and K2 sites converge to 0.480(8) and 0.516(11), respectively. Within one standard deviation, these sum to a total potassium content of 1 per Ir. Thus, the formula of the material made, based on the free occupancy refinement, is taken as 1 K per formula unit. The formula of our material, $KIrO_3$, used for the final refinement, is ideal.

$KIrO_3$ with a primitive cubic cell (*P*-$KIrO_3$) was reported in 1997[24]. The crystal structure of *P*-$KIrO_3$ was refined by those researchers in space group *Pn*-3 (No. 201)[24]. The major difference between primitive *P*-$KIrO_3$ and body centered $KIrO_3$ (*I*-$KIrO_3$) is the distribution of the K atoms in the tunnels. The primitive version has ordered K in the tunnels, in fully occupied sites, while the body centered material, described here, has a larger number of partially occupied K sites. For

comparison, [001] and [110] projections of the K atom distributions for *P*-$KIrO_3$ and *I*-$KIrO_3$ are shown in Figure 5. The K atoms (Wyckoff sites 4*b* and 8*e*) are fully ordered in the crystal structure of *P*-$KIrO_3$. In contrast, the K atoms exhibit a disordered state in the tunnels of *I*-$KIrO_3$ (Wyckoff sites 16*f* and 8*c*). K1 and K2 partially occupy two different crystallographically independent positions in the average structure of *I*-$KIrO_3$. They are thus disordered. We have no information at this time about whether the disorder is static or dynamic. The disordered K distribution in our material is very clearly supported by the K partial difference Fourier map, shown in Figure 4. Our S-XRD refinement results (i.e. the Wyckoff sites of the K ions) for *I*-$KIrO_3$ are in good agreement with those high-pressure studies for *Im*-3-type $KSbO_3$[34] and *Im*-3-type $K_{0.84}OsO_3$[20].

The products from high-pressure synthesis gave us $KIrO_3$ as the main phase, though we did not get single crystals. We did not distinguish primitive from body-centered forms, although the P-XRD patterns obtained were consistent with body-centered cubic symmetry. Hence, we only provide a preliminary description of the high-pressure sample. Future investigations employing high-pressure in situ-XRD may be useful for elucidating the relative structural stabilities of *P*-$KIrO_3$ and *I*-$KIrO_3$. The results could be compared to what is known for *Im*-3 $KSbO_3$ which is reported to remain stable up to 40.5 GPa[34]. Thus, based on our preliminary high-pressure experiments, $KIrO_3$ is a promising system for future high-pressure structural investigation.

The temperature-dependent magnetic susceptibility, $\chi(T)$, of *I*-$KIrO_3$ is shown in Figure 6*a*. No long-range magnetic order is observed over the measured temperature range. A weak upturn is observed on cooling down to 1.8 K, a reflection of the paramagnetic behavior of *I*-$KIrO_3$ in this temperature range. Similar paramagnetic behavior was observed in *P*-$KIrO_3$[24]. The low temperature susceptibility data are fit based on the Curie-Weiss Law, $\chi(T) = \chi_0 + C/(T - \Theta_{CW})$ (C, Curie Constant; Θ_{CW}, Curie-Weiss temperature; χ_0, temperature independent contribution). The

equation $\mu_{eff} = \sqrt{8C}$ (CGS units) was used for interpreting the effective magnetic moment. The Curie-Weiss fitting between 1.8-8 K gives the parameters: Θ_{CW} = -0.79 K, χ_0 = 1.6× 10^{-4} emu·mol^{-1}·Oe^{-1} and μ_{eff} = 0.12 μ_B/Ir. The temperature independent contribution to the susceptibility, χ_0, which dominates the behavior over a wide range of temperature below 300 K, is significant in magnitude. The possible presence of a magnetic impurity was checked by powder XRD. No impurity was found to the sensitivity level of our technique (about 2%) A non-zero effective moment has also been reported in *P*-$KIrO_3$[24] and other Ir^{5+}-based materials (Table 3). The small Θ_{CW} = -0.79 K implies weak antiferromagnetic interactions between the magnetic moments. As shown in Figure 6*b*, nonlinear response is observed in the field-dependent magnetization of *I*-$KIrO_3$ at low temperatures (1.8 K) and high applied fields, which is common in d^4 iridates[27, 35]. In contrast, linear *M* vs. *H* behavior of *I*-$KIrO_3$ is observed at 300 K. The temperature-independent contribution to the magnetic susceptibility, χ_0, is relatively small but positive, estimated to be on the order of 10^{-4} emu·mol^{-1}·Oe^{-1} seen in both the $\chi(T)$ data and the M(*H*) data at high applied fields. This reflects the presence of a positive temperature-independent susceptibility contribution that is added to the core diamagnetism.

To further evaluate the magnetic state of *I*-$KIrO_3$, zero field heat capacity (C_p versus *T*) measurements were performed. No λ-like peaks or broad humps were observed between 1.8 and 150 K (Figure 7); C_p is instead dominated by what is typically seen for phonon contributions to the heat capacity. Hence, long range magnetic order and structural transitions are absent in the measured temperature range, consistent with the behavior observed with $\chi(T)$. C_p/T vs. T^2 for the low temperature range (1.8-10 K), is shown in the Figure 7 inset. This plot allows the determination of the Sommerfeld constant. The expected behavior for C_p at low temperature is: $C_p/T = \gamma + \beta T^2$.

γ, typically associated with the contribution of conduction electrons to the heat capacity at low temperatures, is thus estimated to be approximately 20 mJ/mol·K^2 for *I*-$KIrO_3$, a non-trivial value. We note that deviations from simple expectations for C_p/T vs. T^2 behavior below 10 K are also seen for $La_4Ru_6O_{19}$[36, 37]. Finally, the fact that the heat capacity has not attained a constant value by 150 K suggests that the Debye temperature is higher than that temperature for this material.

It is of particular interest that a small but non-zero effective magnetic moment is observed. Although the interpretation of effective moment values for materials with extended Ir-O networks can be difficult due to electron delocalization, we note that the low effective moment observed for our Ir^{5+} material, which in a localized orbital picture should display a $J_{eff} = 0$ state in a material with Ir^{5+} in an octahedral crystal field with strong spin-orbit coupling, is consistent with what is observed in other Ir^{5+} oxides based on IrO_6 octahedra[13, 25-27, 38, 39]. Some of the properties of these materials are listed in Table 3. To the best of our knowledge, the origin of the non-zero moments in these systems remains under active study.

Different magnetic and electronic properties are found for different materials in the $KSbO_3$ structure family. For additional comparison, the structural information and physical properties of some of the known $KSbO_3$-type materials are summarized in Table 4. Structurally, they all exhibit 3D tunnel-like frameworks made of dimers of edge-sharing octahedra [M_2O_{10}] (M = 3*d*, 4*d* or 5*d* transition elements). The non-magnetic "A" cations with different valence states, such as K^+, Ba^{2+}, Bi^{3+}, and La^{3+} fill in the tunnels. Generally, the quantity of the "guest" A cations is variable, depending on the nature of A, the ratio of starting materials, and the synthesis conditions. The amount and charge of the A ion in turn determines the valence state of the transition metal ions. Hence, the transition metal ions can display a fractional formal valence state, such as $Ir^{+4.67}$ in $Ba_2Ir_3O_9$[23] and $Ir^{+4.33}$ in $La_3Ir_3O_{11}$[21, 22]. Fractional formal valence states in 3*d*-based systems

sometimes lead to charge ordering or charge separation and can make 3*d* systems interesting[42-44]. When 4*d* or even 5*d* transition elements are present in the networks, then the electronic and magnetic properties of the materials are the result of cooperative effects of the SOC, electron correlations, and crystal field splitting.

CONCLUSION

In conclusion, a $KSbO_3$-type 5*d* oxide, BCC $KIrO_3$, was synthesized by the solid-state reaction in a sealed silica tube in an O-rich and K-rich environment. It adopts a body-centered cubic crystal structure with space group *Im*-3. Structurally, it exhibits a 3D tunnel-like framework with disordered K atoms in the tunnels. The two kinds of K sites are partially occupied. The compound contains the formal valence state of Ir = +5. Weak temperature-dependent paramagnetic behavior is observed, with a very low effective moment, consistent with other reports of Ir^{5+} oxides. No long-range magnetic ordering is observed, and the heat capacity data yield a Sommerfeld constant of about 20 mJ/mol·K^2. *I*-$KIrO_3$, as an example of $KSbO_3$-type compounds, is worthy of further study due to its absence of long-range magnetic order and to better understand the properties of 5*d* oxides. The temperature-dependent resistivity will be of particular interest. We speculate that the $KSbO_3$-type crystal structure provides fruitful ground for designing new materials and understanding their physical properties. Larger single crystals, suitable for further characterization, will be needed for a comprehensive understanding of this material.

ASSOCIATED CONTENT

Supporting Information.

The following files are available free of charge.

The crystallographic and crystal structure information for $KIrO_3$.

Accession Codes

The CCDC number containing the supplementary crystallographic data for $KIrO_3$ is 2004529. This data can be obtained free of charge via www.ccdc.cam.ac.uk/data_request/cif, by emailing data_request@ccdc.cam.ac.uk, or by contacting The Cambridge Crystallographic Data Centre, 12 Union Road, Cambridge CB2 1EZ, UK; fax: + 441223336033.

AUTHOR INFORMATION

Corresponding Author

R.J. Cava *E-mail: rcava@princeton.edu

ORCID

Shu Guo: 0000-0002-2098-8904

K.M. Powderly: 0000-0002-0469-5642

R.J. Cava: 0000-0002-3294-6867

Notes The authors declare no competing financial interest.

ACKNOWLEDGMENT

This work was supported by the Institute for Quantum Matter, an Energy Frontier Research Center funded by the U.S. Department of Energy, Office of Science, Basic Energy Sciences under Award No. DE-SC0019331. K.M.P. acknowledges the support of the National Science Foundation Graduate Research Fellowship under Grant No. DGE-1656466.

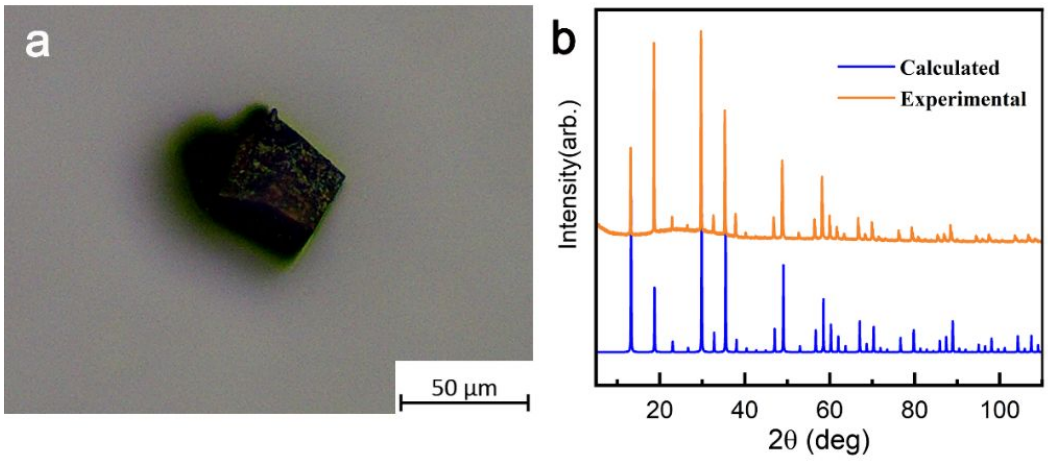

Figure 1. The basic material. (***a***) As-grown single crystal of *I*-$KIrO_3$ and (***b***) the comparison of the experimental P-XRD pattern and calculated XRD pattern (simulated pattern from the S-XRD).

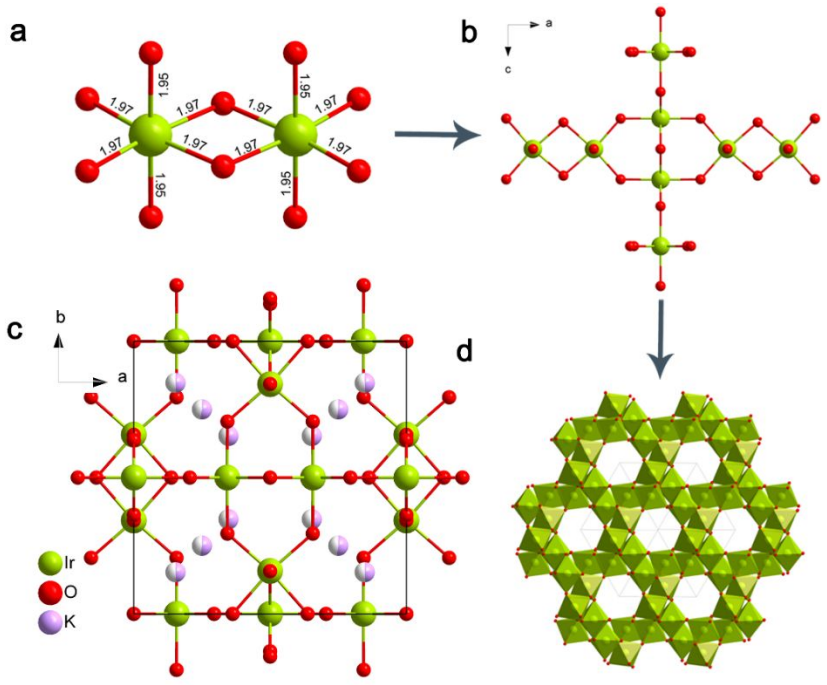

Figure 2. Crystal structure of BCC $KIrO_3$ at 100 K. (***a***) $[Ir_2O_{10}]$ dimer based on edge-sharing octahedra $[IrO_6]$ with Ir−O bond lengths *d*(Ir−O) = 1.94-1.97 Å, (***b***) 3D geometrical framework constructed via interconnected $[Ir_2O_{10}]$ dimers in the *ac*-plane, (***c***) unit cell of *I*-$KIrO_3$, and (*d*) 3D tunnel-like framework viewed along the [111] direction.

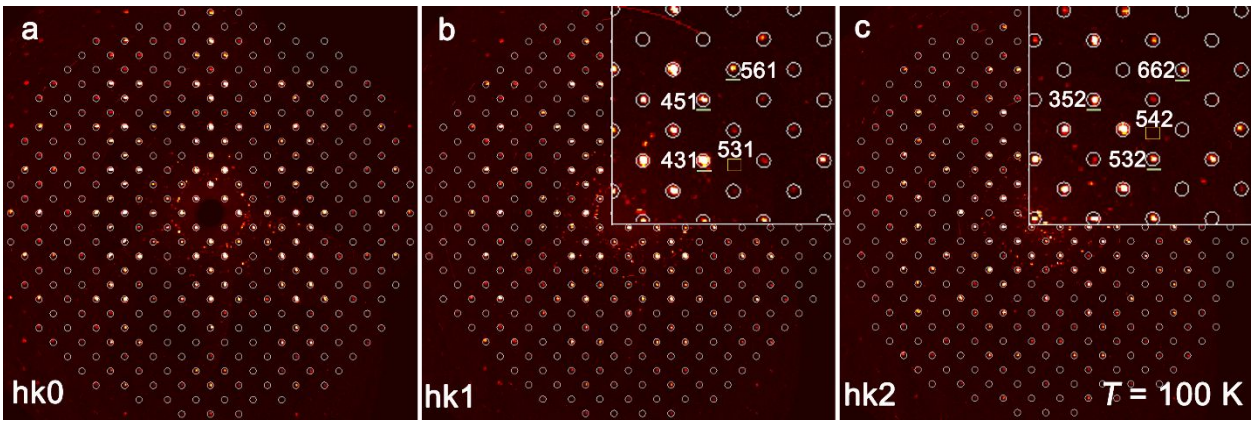

Figure 3. The first three reciprocal lattice planes as determined by S-XRD at 100 K. (***a***) *hk*0, (***b***) *hk*1 and (***c***) *hk*2 reciprocal lattice planes. The circled diffraction peaks meet the requirement that $h + k + l = 2n$ (n = integer)) for a body-centered material. Insets in *b* and ***c***: The 531 and 542 reflections are absent (empty squares). These are two of the three strongest peaks reported to violate the body centering conditions for the primitive structure material.

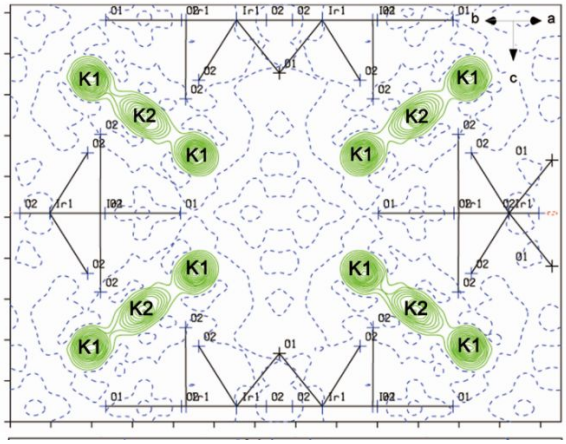

Figure 4. Potassium partial difference Fourier map for *I*-$KIrO_3$ in the (110) plane. The K atoms in the tunnel have been deleted from the final structure refinement to generate a F_{Obs}-F_{Calc} difference Fourier map, which clearly shows the positions of K atoms (as marked).

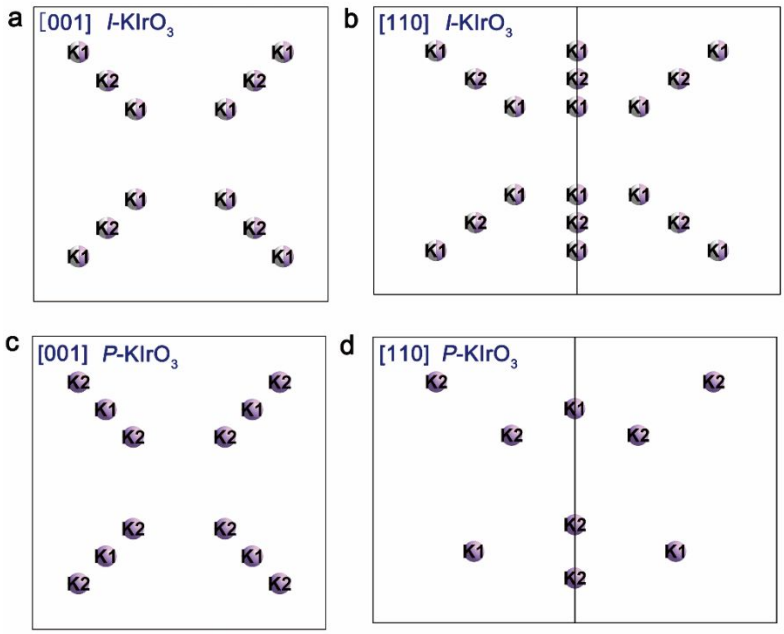

Figure 5. [001] and [110] projections of the refined positions of the K atoms in the tunnels in body centered cubic *I*-$KIrO_3$ **(*a,b*)** and primitive cubic *P*-$KIrO_3$ (***c,d***) (ICSD 4200), respectively. The coordinates for atoms for *P*-$KIrO_3$ have been shifted to origin choice 1 of space group 201 to facilitate the comparison (the original report employs origin choice 2). For the primitive structure material all K sites are fully occupied. For the body centered structure material each site is about half occupied (see the refinement results).

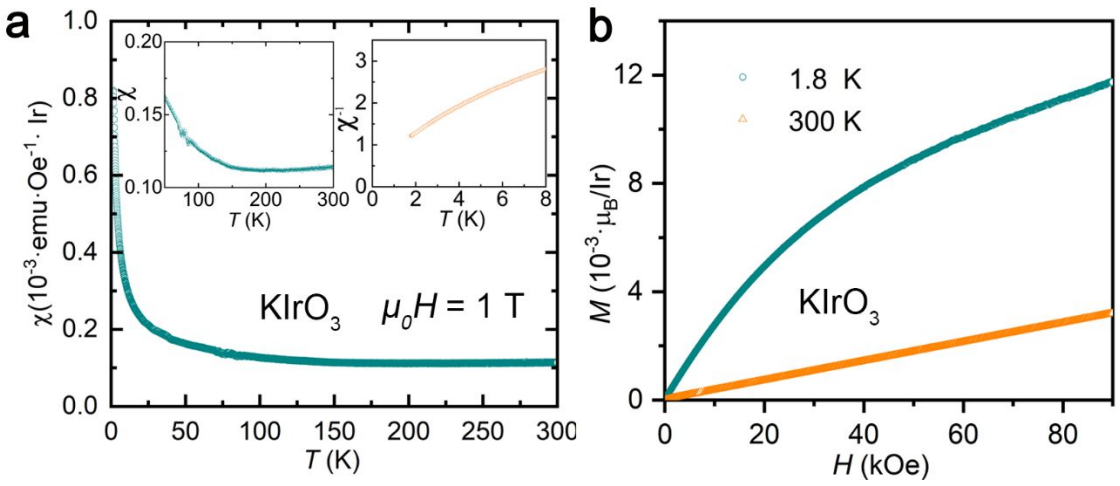

Figure 6. Magnetic characterization of BCC $KIrO_3$. (***a***) temperature-dependent magnetic susceptibility (green), $\chi(T)$, measured at $\mu_0 H = 1$ T and inverse magnetic susceptibility (orange), $\chi^{-1}(T)$ and (***b***) field-dependent magnetization measurements at 1.8 K (green) and 300 K (orange) based on the powder sample. Inset 6***a*** left shows the $\chi(T)$ in the high temperature range (50-300 K) and inset 6***a*** right shows linear behavior of $\chi^{-1}(T)$ vs T.

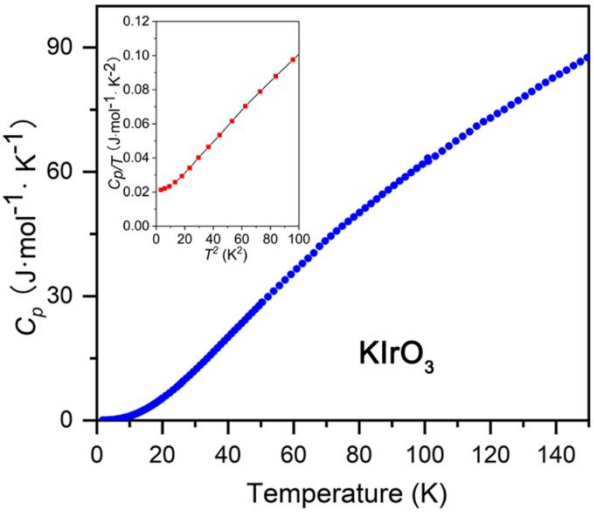

Figure 7. Heat capacity characterization of BCC $KIrO_3$. Temperature dependence of the heat capacity $C_p(T)$ in the wide temperature range (1.8-150 K). Inset shows the C_p/T vs T^2 data in the temperature range of 1.8-10 K.

Table 1. Crystallographic data for *I*-$KIrO_3$ at 100 (K).

T (K)	100(1)
formula mass(amu)	279.30
crystal system	cubic
space group	*Im*-3
a(Å)	9.4465(3)
V(Å^3)	842.97(4)
Z	12
ρ*(calcd)(g/cm^3)*	6.602
λ (Å)	0.71073
F(000)	1440
θ*(deg)*	3.05-33.03
Cryst size (mm^3)	0.028 × 0.024 × 0.020
μ(mm^{-1})	48.753
Final R indices (R_1/ωR_2)	0.0125/0.0296
R indices (all data) (R_1/ωR_2)	0.0132/0.0298
Residual electron density/ (eÅ^{-3})	(-1.073) - 2.297
Goodness of fit	1.294

Table 2. Wyckoff positions, coordinates, occupancies, and equivalent isotropic displacement parameters respectively for *I*-$KIrO_3$ at 100 K.

Atoms	Wyck.Site	x	y	z	S.O.F.	U_{eq}
Ir1	12*e*	0.15741(2)	0	1/2	1	0.00167(7)
K1	16*f*	0.1529(2)	0.1529(2)	0.1529(2)	0.489(5)	0.0172(6)
K2	8*c*	1/4	1/4	1/4	0.523(9)	0.0383(18)
O1	12*d*	0.3627(4)	0	0	1	0.0039(7)
O2	24*g*	0	0.3433(3)	0.2945(3)	1	0.0056(5)

Table 3 Structural and magnetic comparison of some known Ir^{5+} compounds.

Material	μ_{eff} (μ_B/Ir)	Θ_{CW} (K)	**Structural motif**	**Connectivity of IrO_6**
$Ba_3CdIr_2O_9$[27]	~ 0.3	−21	Hexagonal perovskite	Face-sharing
$Ba_3ZnIr_2O_9$[25]	~0.2	-30	Hexagonal perovskite	Face-sharing
$BaSrYIrO_6$[38]	~0.4	-2(1)	Double perovskite	Isolated
Ba_2ScIrO_6[26]	0.39	~0	Double perovskite	Isolated
Sr_2YIrO_6[39]	0.91	-229	Double perovskite	Isolated
$Sr_3CaIr_2O_9$[13]	0.18	-8(5)	Honeycomb lattice	Corner-sharing
$NaIrO_3$[13]	0.18	0(2)	Honeycomb lattice	Edge-sharing
I-$KIrO_3$*	0.12	-0.79	3D tunnel	Edge-sharing and corner-sharing

* = This work.

Table 4. Structural and magnetic comparison of selected $KSbO_3$-family materials.

Compound	**Formal transition metal oxidation state**	**Space group**	**Unit cell parameter** (a, Å)	**Basic properties**
$Bi_3Mn_3O_{11}$[40]	Mn+4.33	*Pn*-3 (RT, S)	9.16	Ferrimagnet
$Bi_3Ru_3O_{11}$[19, 41]	Ru+4.33	*Pn*-3 (RT, P)	9.31	Non-Fermi liquid
$La_4Ru_6O_{19}$[36, 37]	Ru+4.33	*I*23 (RT, S)	8.98	Non-Fermi-liquid
$Ba_2Ir_3O_9$[23]	Ir+4.67	*I*23 (RT, P)	9.42	Metal, paramagnet
$La_3Ir_3O_{11}$[21, 22]	Ir+4.33	*Pn-3* (RT, P)	9.49	Mott insulator, paramagnet
I-$KIrO_3$*	Ir+5	*Im*-3 (100K, S)	9.46	Paramagnet
$K_{0.84}OsO_3$[20]	Os+5.16	*Im*-3 (RT, P)	9.47	Metal, paramagnet
$Bi_{2.93}Os_3O_{11}$[20]	Os+4.40	*Pn*-3 (RT, P)	9.36	Metal, paramagnet

S refers to S-XRD refinement and P refers to P-XRD refinement; RT refers to room temperature.
* = This work.

REFERENCE

1. C. N. R. Rao, *Annu. Rev. Phys. Chem*. **1989**, *40*, 291-326.
2. K. Luo, M. R. Roberts, R. Hao, N. Guerrini, D. M. Pickup, Y.-S. Liu, K. Edström, J. Guo, A. V. Chadwick and L. C. Duda, *Nat. Chem.* **2016,** *8*, 684.
3. X.-Y. Wang, C. Avendaño and K. R. Dunbar, *Chem. Soc. Rev.* **2011,** *40*, 3213-3238.
4. C. Gang, *Frontiers of 4D-and 5D-transition Metal Oxides*, World Scientific, 2013.
5. C. Martins, M. Aichhorn and S. Biermann, *J. Phys-condens Mat.* **2017,** *29*, 263001.
6. S. Guo, R. Zhong, W. Wang, J. Tao, D. Ni and R. J. Cava, *J. Am. Chem. Soc.* **2020,** *142*, 5389-5395.
7. G. Cao, V. Durairaj, S. Chikara, S. Parkin and P. Schlottmann, *Phys. Rev. B* **2007,** *75*, 134402.
8. S. Nishimoto, V. M. Katukuri, V. Yushankhai, H. Stoll, U. K. Rößler, L. Hozoi, I. Rousochatzakis and J. Van Den Brink, *Nat. Commun.* **2016,** *7*, 10273.
9. V. M. Katukuri, R. Yadav, L. Hozoi, S. Nishimoto and J. Van Den Brink, *Sci. Rep.* **2016,** *6*, 29585.
10. M. Abramchuk, C. Ozsoy-Keskinbora, J. W. Krizan, K. R. Metz, D. C. Bell and F. Tafti, *J. Am. Chem. Soc.* **2017,** *139*, 15371-15376.
11. S. K. Takahashi, J. Wang, A. Arsenault, T. Imai, M. Abramchuk, F. Tafti and P. M. Singer, *Phys. Rev. X* **2019,** *9*, 031047.
12. A. Shitade, H. Katsura, J. Kuneš, X.-L. Qi, S.-C. Zhang and N. Nagaosa, *Phys. Rev. Lett.* **2009,** *102*, 256403.
13. D. C. Wallace and T. M. McQueen, *Dalton T.* **2015,** *44*, 20344-20351.
14. Z. Tian, Y. Kohama, T. Tomita, H. Ishizuka, T. H. Hsieh, J. J. Ishikawa, K. Kindo, L. Balents and S. Nakatsuji, *Nat. Phys.* **2016,** *12*, 134-138.
15. M. C. Shapiro, S. C. Riggs, M. B. Stone, C. R. de la Cruz, S. Chi, A. A. Podlesnyak and I. R. Fisher, *Phys. Rev. B* **2012,** *85*, 214434.
16. S. Calder, J. G. Vale, N. Bogdanov, X. Liu, C. Donnerer, M. Upton, D. Casa, A. Said, M. Lumsden and Z. Zhao, *Nat. Commun.* **2016,** *7*, 1-8.
17. X. Wan, A. Vishwanath and S. Y. Savrasov, *Phys. Rev. Lett* **2012,** *108*, 146601.
18. K. Kojima, R. Kadono, M. Miyazaki, M. Hiraishi, I. Yamauchi, A. Koda, Y. Tsuchiya, H. Suzuki and H. Kitazawa, *Phys. Rev. Lett*. **2014,** *112*, 087203.
19. T. Fujita, K. Tsuchida, Y. Yasui, Y. Kobayashi and M. Sato, *Physica B* **2003,** *329*, 743-744.
20. Y. Yuan, H. L. Feng, Y. Shi, Y. Tsujimoto, A. A. Belik, Y. Matsushita, M. Arai, J. He, M. Tanaka and K. Yamaura, *Sci. Technol. Adv. Mat.* **2014,** *15*, 064901.
21. T. Aoyama, K. Emi, C. Tabata, Y. Nambu, H. Nakao, T. Yamauchi and K. Ohgushi, *J. Phys. Soc. Jpn.* **2019,** *88*, 093706.
22. J. Yang, J. Wang, W. Zhen, L. Ma, L. Ling, W. Tong, C. Zhang, L. Pi and W. Zhu, *Phys. Rev. B* **2019,** *100*, 205107.
23. Y. Kawamura and H. Sato, *J. Alloy. Compd.* **2004,** *383*, 209-212.
24. R. Hoppe and K. Claes, *J. less-common Met.* **1975,** *43*, 129-142.
25. A. Nag, S. Middey, S. Bhowal, S. K. Panda, R. Mathieu, J. Orain, F. Bert, P. Mendels, P. G. Freeman and M. Mansson, *Phys. Rev. Lett.* **2016,** *116*, 097205.
26. P. Kayser, B. J. Kennedy, B. Ranjbar, J. A. Kimpton and M. Avdeev, *Inorg. Chem.* **2017,** *56*, 2204-2209.

27. M. S. Khan, A. Bandyopadhyay, A. Nag, V. Kumar, A. Mahajan and S. Ray, *Phys. Rev. B* **2019,** *100*, 064423.
28. J. B. Goodenough, *J. Solid State Chem.* **1973,** *6*, 493-501.
29. G. M. Sheldrick, *Acta Crystallogr. C* **2015,** *71*, 3-8.
30. L. J. Bourhis, O. V. Dolomanov, R. J. Gildea, J. A. Howard and H. Puschmann, *Acta Crystallogr. A* **2015,** *71*, 59-75.
31. O. V. Dolomanov, L. J. Bourhis, R. J. Gildea, J. A. Howard and H. Puschmann, *J. Appl. Crystallogr.* **2009,** *42*, 339-341.
32. A. Spek, *J. Appl. Crystallogr.* **2003,** *36*, 7-13.
33. H.-P. Hong, J. Kafalas and J. B. Goodenough, *J. Solid State Chem.* **1974,** *9*, 345-351.
34. H. Zhao, D. Tan, Y. Tian, Y. He, Y. Li, X. Li, K. Yang, B. Chen and W. Xiao, *High Pressure Res.* **2018,** *38*, 232-242.
35. T. Dey, A. Maljuk, D. Efremov, O. Kataeva, S. Gass, C. Blum, F. Steckel, D. Gruner, T. Ritschel and A. Wolter, *Phys. Rev. B* **2016,** *93*, 014434.
36. P. Khalifah and R. J. Cava, *Phys. Rev. B* **2001,** *64*, 085111.
37. P. Khalifah, K. Nelson, R. Jin, Z. Mao, Y. Liu, Q. Huang, X. Gao, A. Ramirez and R. J. Cava, *Nature* **2001,** *411*, 669-671.
38. B. F. Phelan, E. M. Seibel, D. Badoe Jr, W. Xie and R. J. Cava, *Solid State Commun.* **2016,** *236*, 37-
39. G. Cao, T. Qi, L. Li, J. Terzic, S. Yuan, L. E. DeLong, G. Murthy and R. K. Kaul, *Phys. Rev. Lett.* **2014,** *112*, 056402.
40. A. A. Belik and E. Takayama-Muromachi, *J. Am. Chem. Soc.* **2009,** *131*, 9504-9505.
41. F. Abraham, D. Thomas and G. Nowogrocki, *Bull. Minéral.* **1975,** *98*, 25-29.
42. D. V. Efremov, J. Van Den Brink and D. I. Khomskii, *Nat. Mater.* **2004,** *3*, 853-856.
43. M. Coey, *Nature* **2004,** *430*, 155-157.
44. T. Goto and B. Lüthi, *Adv. Phys.* **2003,** *52*, 67-118.

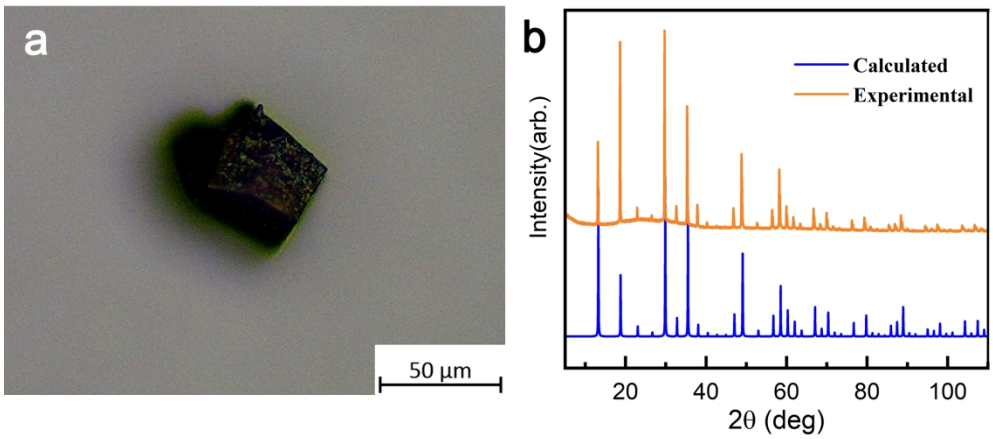

Figure 1. The basic material. (a) As-grown single crystal of *I*-$KIrO_3$ and (b) the comparison of the experimental P-XRD pattern and calculated XRD pattern (simulated pattern from the S-XRD).

1024x475mm (72 x 72 DPI)

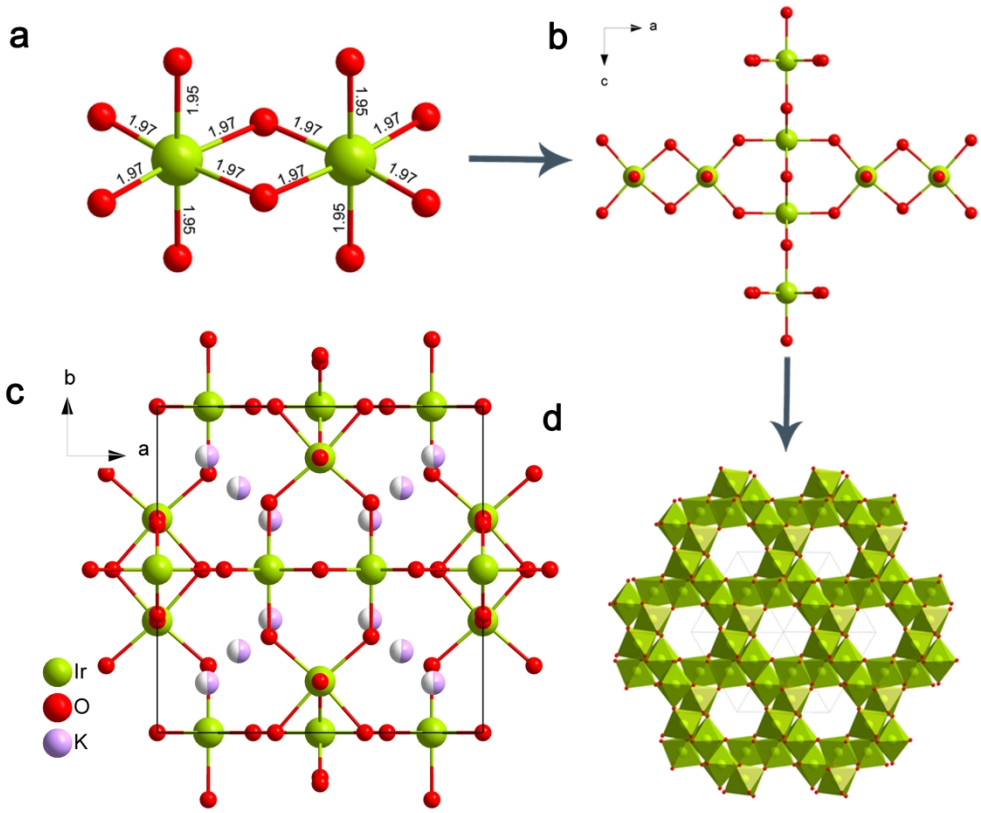

Figure 2. Crystal structure of BCC $KIrO_3$ at 100 K. (a) $[Ir_2O_{10}]$ dimer based on edge-sharing octahedra $[IrO_6]$ with Ir−O bond lengths d(Ir−O) = 1.94-1.97 Å, (b) 3D geometrical framework constructed via interconnected $[Ir_2O_{10}]$ dimers in the ac-plane, (c) unit cell of $KIrO_3$, and (d) 3D tunnel-like framework viewed along the [111] direction.

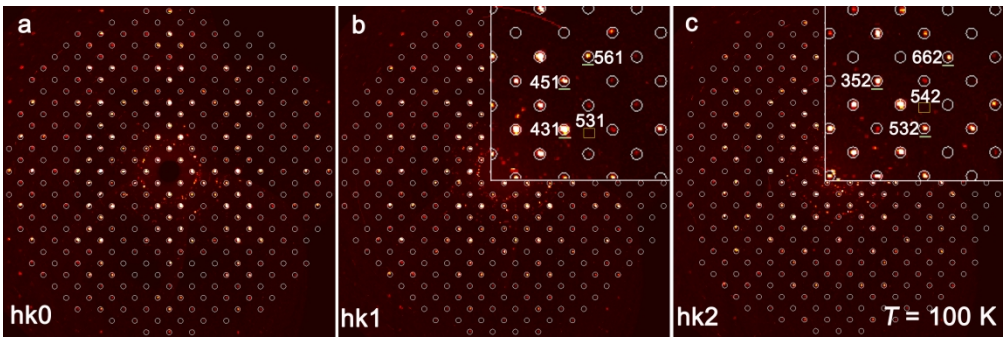

Figure 3. The first three reciprocal lattice planes as determined by S-XRD at 100 K. (a) hk0, (b) hk1 and (c) hk2 reciprocal lattice planes. The circled diffraction peaks meet the requirement that h + k+ l = 2n (n = integer)) for a body-centered material. Insets in *b* and *c*: The 531 and 542 reflections are absent (empty squares). These are two of the three strongest peaks reported to violate the body centering conditions for the primitive structure material.

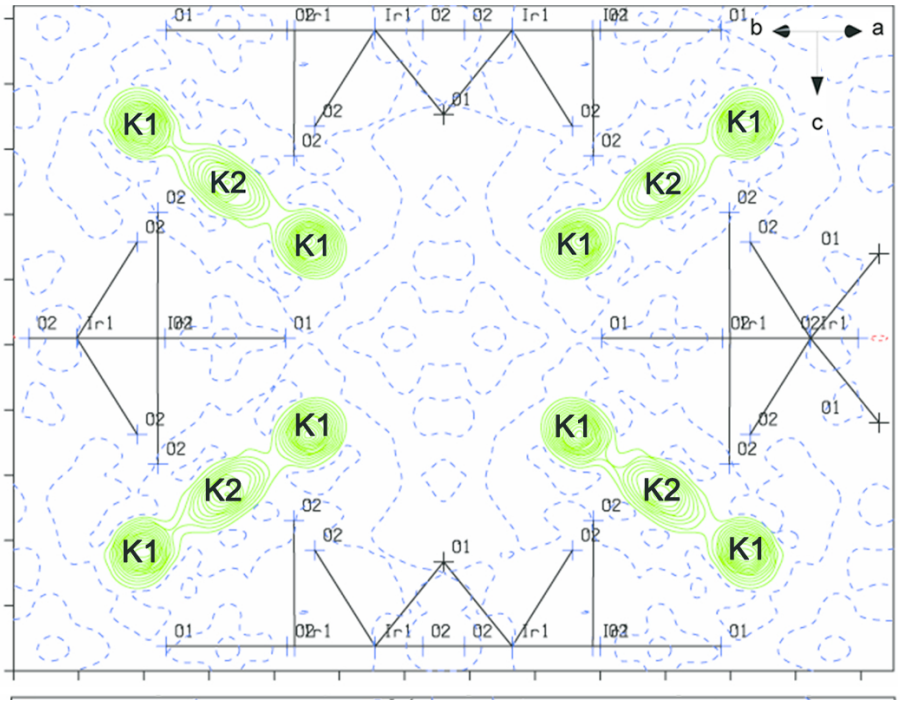

Figure 4. Potassium partial difference Fourier map for *I*-KIrO3 in the (110) plane. The K atoms in the tunnel have been deleted from the final structure refinement to generate F_{Obs}-F_{Calc} difference Fourier Map, which clearly show the positions of K atoms (as marked).

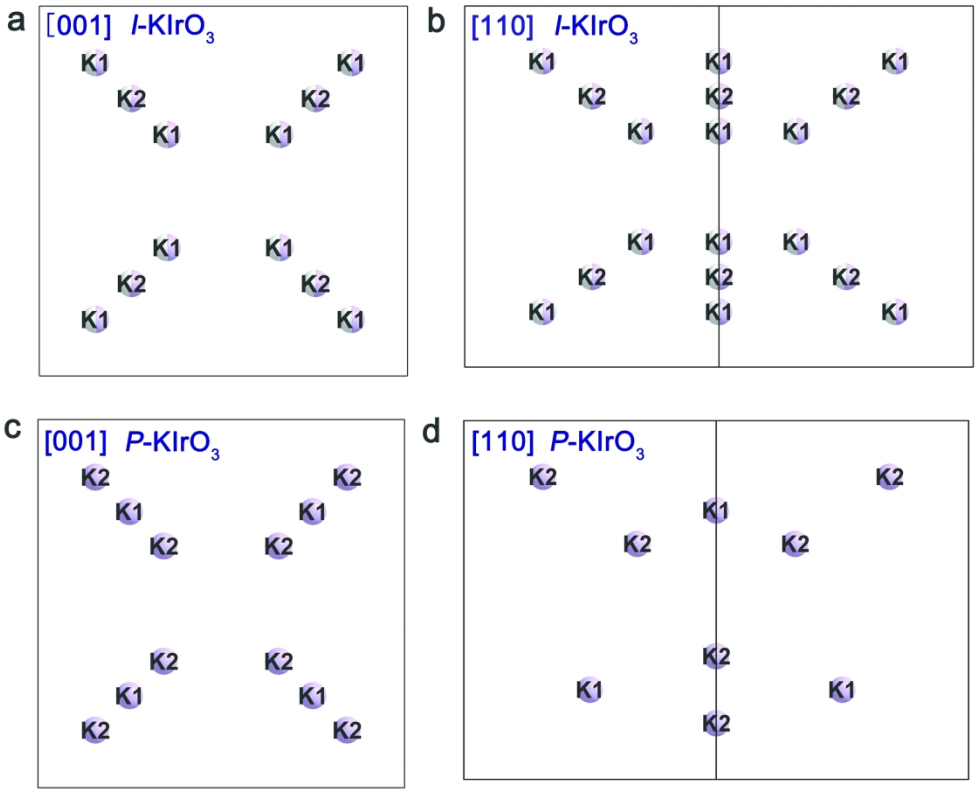

Figure 5. [001] and [110] projections of the refined positions of the K atoms in the tunnels in body centered cubic I-$KIrO_3$ (a,b) and primitive cubic P-$KIrO_3$ (c,d) (ICSD 4200), respectively. The coordinates for atoms for P-$KIrO_3$ have been shifted to origin choice 1 of space group 201 to facilitate the comparison (the original report employs origin choice 2). For the primitive structure material all K sites are fully occupied. For the body centered structure material each site is about half occupied (see the refinement results).

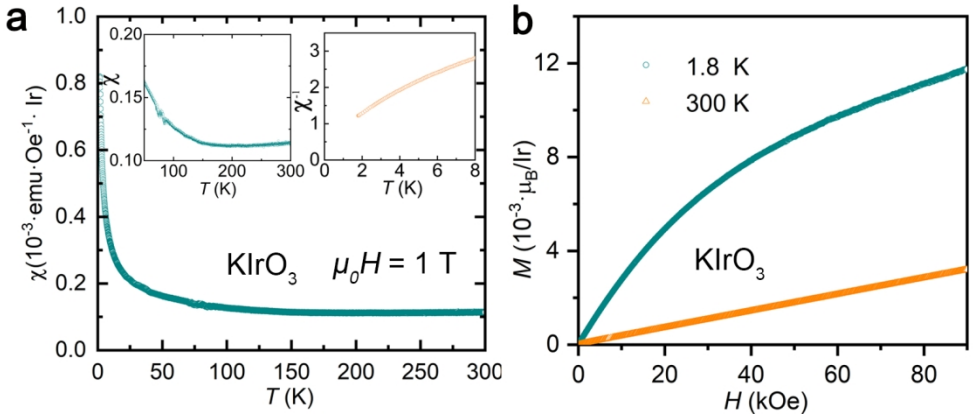

Figure 6. Magnetic characterization of BCC $KIrO_3$. (a) temperature-dependent magnetic susceptibility (green), χ(T), measured at μ_0H = 1 T and inverse magnetic susceptibility (orange), χ^{-1}(T) and (b) field-dependent magnetization measurements at 1.8 K (green) and 300 K (orange) based on the powder sample. Inset 6a left shows the χ(T) in the high temperature range (50-300 K) and inset 6a right shows linear behavior of χ^{-1}(T) vs T.

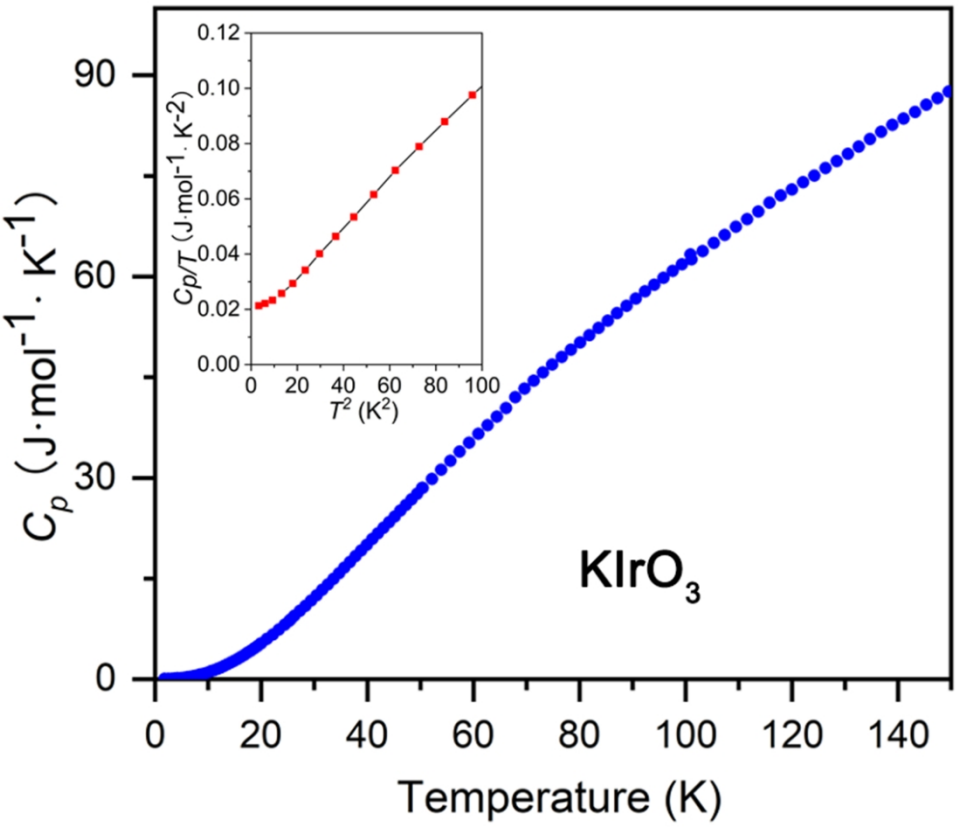

Figure 7. Heat capacity characterization of BCC KIrO3. Temperature dependence of the heat capacity $C_p(T)$ in the wide temperature range (1.8-150 K). Inset shows the C_p/T vs T^2 data in the temperature range of 1.8-10 K.

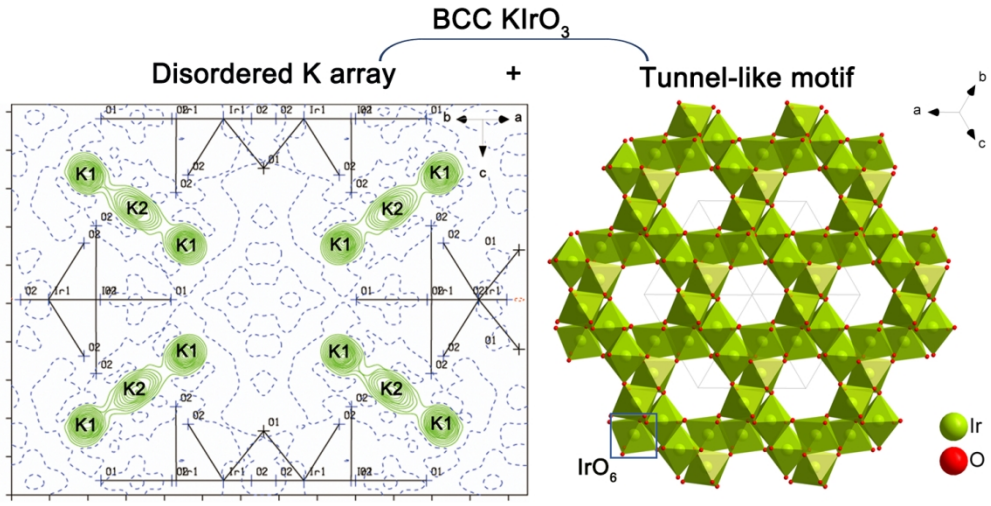
BCC KIrO3
Disordered K array
+
Tunnel-like motif
K1
K2
IrO6
Ir
O